Materials Science & Engineering A 809 (2021) 140951

Contents lists available at ScienceDirect

Materials Science & Engineering A

journal homepage: http://www.elsevier.com/locate/msea

Microstructure, heat treatment and mechanical properties of TiB_2/Al–7Si–Cu–Mg alloy fabricated by selective laser melting

Y.K. Xiao [a,b], Q. Yang [a,b], Z.Y. Bian [a,b], H. Chen [a,b], Y. Wu [b,*], Q. Lian [b], Z. Chen [b,**], H.W. Wang [a]

[a] State Key Laboratory of Metal Matrix Composites, Shanghai Jiao Tong University, No. 800 Dongchuan Road, Shanghai, 200240, China
[b] School of Materials Science & Engineering, Shanghai Jiao Tong University, No. 800 Dongchuan Road, Shanghai, 200240, China

ARTICLE INFO

Keywords:
Selective laser melting
Aluminium alloys
Heat treatment
Microstructure
Mechanical properties

ABSTRACT

Selective laser melting (SLM) of aluminium alloys is of research interest due to its potential benefits in fabricating complex components for aerospace and automotive industries. In order to improve the mechanical properties and demonstrate the credibility of selective laser melted (SLMed) Al alloys, the effects of post heat treatment on the microstructures and mechanical properties need to be studies. In the present work, the nano-TiB_2 decorated Al–7Si–Cu–Mg samples were successfully fabricated using the SLM technique, and then post-treated by direct ageing and conventional T6 heat treatment. The as-built TiB_2/Al–7Si–Cu–Mg sample exhibits fine equiaxed grain structures without preferred crystallographic texture due to the high cooling rate of SLM and the addition of nano-TiB_2 particles. Nano-scale eutectic Si cells are present within the equiaxed grains. Inside the cells, there are dislocation tangles without precipitates. After direct ageing treatment, the grain and cell structures remain almost unchanged, and the new Al_2Cu, Mg_2Si, and Si phases are formed around the dislocations. While after T6 treatment, the fine grains grow up and the eutectic Si phases coarse leading to the broken of cell structures. Besides, the as-built TiB_2/Al–7Si–Cu–Mg samples show high tensile strength and ductility (yield strength: 297.2 MPa, ultimate tensile strength: 474.6 MPa, elongation: 13.4%). During ageing, the yield strength is enhanced by ~35% due to precipitation hardening effect. While the broken of fine microstructure during T6 leads to the decrease of yield strength by ~16%. The microstructure development and preliminary strengthening mechanism were discussed. The effect of post-heat treatments can yield the SLMed TiB_2/Al–7Si–Cu–Mg samples with appropriate mechanical properties, promoting a wide range of applications.

1. Introduction

As an emerging technology, additive manufacturing (AM), also known as 3D printing, promises to revolutionize manufacturing by rapidly fabricating three-dimensional solid objects with complex and customized geometries layer-by-layer [1]. Selective laser melting (SLM), the most popular process of metal AM, is a laser powder bed fusion process able to produce robust metallic structures [2,3]. It is of great interests in investigating the feasibility of manufacturing several different alloys including Ti–6Al–4V [4–6], stainless steel [7–9], nickel-based superalloys [10–12], Al–Si–Mg alloys [13–16], and numerous other advanced alloys.

In recent years, aluminium alloys, especially Al–Si–Mg alloys, are attracting the attention of SLM researchers because of their wide applications in aerospace and automotive industries [17,18]. However, the mechanical properties, especially poor strength, cannot satisfy the requirements in some special fields. Preliminary studies revealed that subsequent heat treatments may be a solution to this problem [18]. To optimize the mechanical properties by application of post heat treatment, it is essential to understand the development of the microstructures and the associated properties during the heat processing.

Up to now, a few studies have discussed the effects of post processing heat treatments in achieving desirable microstructure and mechanical properties [19–28]. The original intention of post heat treatment may be different, to eliminate the high residual stress, to modify the microstructural inhomogeneity or to improve the mechanical properties of the SLMed parts. However, for enhancing strength, most previous studies have focused on the effects of conventional T6 heat treatment (solution treatment and subsequent ageing) on the microstructure and mechanical properties of SLMed Al alloys [27,29], since Al–Si–Mg series alloys (the

* Corresponding author.
** Corresponding author.
E-mail addresses: eagle51@sjtu.edu.cn (Y. Wu), zhe.chen@sjtu.edu.cn (Z. Chen).

https://doi.org/10.1016/j.msea.2021.140951
Received 8 December 2020; Received in revised form 4 February 2021; Accepted 11 February 2021
Available online 16 February 2021

most commonly used alloys for SLM) are recognized as being age-hardenable alloys. Considering the high cooling rate, normally from 10^4K/s to 10^6 K/s [14], of SLM process, the rapid solidification results in the enhanced solubility of Si and Mg elements. Similar to quenching in water following solution treatment of the traditional T6 process, a supersaturated solid solution is formed in the Al matrix. Consequently, direct artificial ageing may be an effective method to enhance the strength. Thus, in this paper, we will compare the influence of conventional T6 and direct ageing treatment, and focus on the microstructure development and the response of mechanical properties.

Additionally, the large columnar grains with preferential texture (normally <001> fiber in FCC Al) that are often formed in SLMed components can significantly degrade the mechanical properties. In our previous studies, we successfully achieved columnar to equiaxed transition using an *in-situ* nano-TiB_2 grain refiner based on the understanding of the evolution of grain structure [14,30]. In general, previous studies (including ours) have not included an analysis of the effects of post heat treatment on the microstructure with SLMed TiB_2/Al–Si alloy. Consequently, a comprehension study of the influence of different thermal processing on the microstructure development and mechanical properties of TiB_2/Al–Si samples is required.

In the present study, to better understand the microstructure development of SLMed *in situ* nano-TiB_2/Al–7Si–Cu–Mg alloy during post heat treatment, the microstructures of as-built, direct ageing and T6 treated samples were examined using X-ray diffraction (XRD), electron backscatter diffraction (EBSD), scanning (SEM) and transmission electron microscopy (TEM). The mechanical properties of the specimens under different treated states were investigated by conducting tensile testing. This paper mainly focused on the issues about the microstructure evolution during heat treatment and the effects of the microstructural characteristics on the mechanical properties.

2. Experimental procedure

2.1. Materials

In the present study, the original powder material of the *in-situ* nano-TiB_2 decorated Al–7Si–Cu–Mg (TiB_2/Al–7Si–Cu–Mg) alloy was successfully synthesized through the salt-metal reaction and gas-atomization as described in Refs. [14,30,31]. Fig. 1a shows the morphology of the alloy powders. The agglomeration of the powder is not observable. The powders are spherical in shape, and some are with small satellites. As shown in Fig. 1b, some nano-TiB_2 particles are distributed on the surface of TiB_2/Al–7Si–Cu–Mg powder. Fig. 1c gives the powder size distribution revealing the powder has a particle size of 20–60 μm. The chemical composition of the alloy powder and SLMed sample measured by ICP-AES (Inductively Couple Plasma Atomic Emission Spectroscopy, iCAP6300) are summarized in Table 1. It can be seen that the proportions of the main alloy elements (Si, Cu and Mg) in the SLMed bulk samples are almost the same as those in the initial powders. Before the SLM process, the powders were first dried in a furnace oven at 70 °C for 24 h.

2.2. SLM process

The SLM processing was carried out at room temperature using a Prox DMP 200 SLM machine (3D System, USA) with a high-purity inert Ar atmosphere to prevent oxidation (oxygen-content < 20 ppm). After a series of preliminary parameters optimization, the 80 × 10 × 10 mm^3 and 10 × 10 × 10 mm^3 cubic samples (Fig. 2a) for tensile testing and microstructure characterization, respectively, were fabricated using laser power of 200 W, scanning speed of 1200 mm/s, hatching space of 100 μm, the layer thickness of 30 μm and scanning strategy of rotation for 90° between layers.

2.3. Heat treatment

After fabrication, the specimens were cut from the base plate using wire cut electric discharge machine. Then, parts of the specimens were subjected to direct ageing followed by air cooling. The direct ageing condition was chosen according to the microhardness evolution at low treated temperature of 150 °C (Fig. 2d). The maximum microhardness state at the temperature of 150 °C for 12 h was chosen as the direct ageing condition. Part of the specimens underwent T6 treatment. The traditional T6 treatment included solution heat treatment at 520 °C for 1 h followed by water quenching in 25 °C water and subsequent artificially ageing at 160 °C for 6 h [29,32].

2.4. Microstructure characterization

The samples were prepared for characterization using various methods. As shown in Fig. 2a, characterization was performed on the side view of the cubic samples. The bulk specimens were mechanically polished and etched with Keller's regent (2.5 vol% HNO_3, 1.5 vol% HCl, 1 vol% HF, 95 vol% H_2O) for 60s. The microstructures were examined using scanning electron microscope (SEM, TESCAN MAIA3). In order to analyze the size of the sub-cell structure of SLMed samples, an image processing approach was adopted using Image J software. For each sample, at least three SEM images were selected to get the representative results. For observation by electron backscatter diffraction (EBSD), the samples were mechanically grinded and ion polished using a Leica EM TIC 3X machine. They were then characterized using a step size of 0.15 μm on a BRUKER e-Flash^{HR} EBSD detector. The data was post treated using CHANNEL 5.0 software package. The thin samples for transmission electron microscope (TEM) observations were prepared by mechanical polishing, ion thinning using a Precision Ion Polishing System (Gatan Model 691) and examined using an FEI Talos F200X microscope operated at 200 kV.

Phase determination of SLMed samples was done by X-ray diffraction (XRD, Ultima IV X-ray diffractometer) with Cu Ka radiation (λ = 0.1542 nm) setting in the 2θ range from 20° to 50° and scanning speed of 2°/min. To determine the dislocation density of the sample, synchrotron

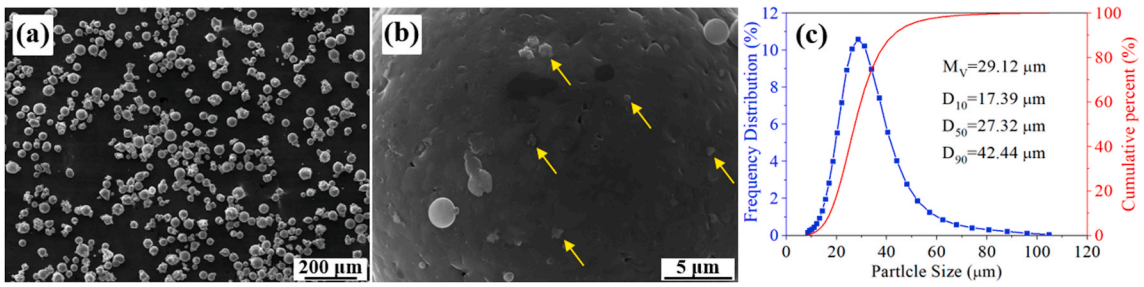

Fig. 1. (a) Typical SEM image of the morphology of TiB_2/Al–7Si–Cu–Mg powders, (b) The surface of the powder in (a), (c) The powder size distribution. Yellow arrows in (b) point to the TiB_2 particles on the surface of the powder. (For interpretation of the references to colour in this figure legend, the reader is referred to the Web version of this article.)

Table 1
The chemical compositions of TiB_2/Al–7Si–Cu–Mg alloy determined by ICP-AES (wt.%).

Element	Si	Cu	Mg	Fe	Ti	B	Al
Powder	7.055	0.8860	0.3905	0.0721	1.432	0.6518	Balance
SLMed sample	7.081	0.8757	0.3402	0.0770	1.413	0.6259	Balance

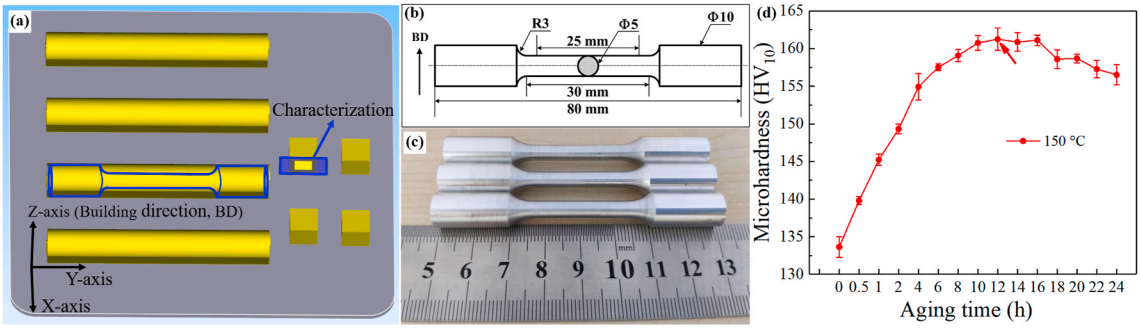

Fig. 2. (a) Schematic illustration of SLMed samples, (b) schematic illustration of the tensile specimen, (c) tensile specimens after machining, (d) the micro-hardness varies versus aging time at 150 °C.

radiation X-ray diffraction (SRXRD) was tested at the Shanghai Synchrotron Radiation Facility (SSRF). The energy of the beam is 18 keV and the wavelength is 0.06889 nm. The SRXRD data was post analysed using the method for the evaluation of dislocation density proposed by Borbely and Groma [33]. The dislocation density is taken as the average of (111), (200), (220) and (311) peaks. The average dislocation density is determined by analysing the asymptotic behaviour of the second-order and fourth-order restricted moments using the restricted moment method.

2.5. Mechanical properties

According to the ASTM-E8M standard, as the configuration shown in Fig. 2b, the dog-bone tensile testing bars were machined (Fig. 2c). The tensile testing was performed at room temperature in the air on a Zwick/Roell Z100 machine at a constant strain rate of 1×10^{-4} s^{-1}. At least three specimens were used for each tensile test condition, and the standard deviation were given.

3. Results

3.1. XRD analysis

Fig. 3 exhibits the XRD patterns of the SLMed TiB_2/Al–7Si–Cu–Mg alloy under as-built state and after direct ageing or T6 heat treatment. It can be seen that every pattern shows peaks corresponding to the face-centered cubic (FCC) α-Al, the diamond-like cubic Si phase and the hexagonal TiB_2 phase. In the as-built samples, no other phases can be detected, which is in consistent with the previous literature [13]. The patterns of direct aged conditions show almost the same peaks with as-built ones. However, by amplifying the patterns between 36° and 49° shown in Fig. 3b, it can be clearly seen that the major Al peaks of (111) and (200) shifted towards the lower diffraction angles in the samples after direct ageing and T6 treatment. According to the Bragg's equation,

$$2d\ sin\theta = n\lambda\ \ (n = 1, 2, 3\ldots) \quad (1)$$

the observed shift suggests an increase in the Al lattice parameter after heat treatment. During the rapid solidification of SLM, there is super solute especially Si in the α-Al matrix. Because the radii of Al and Si are related, it is easier to form the displacement solid solution than the interstitial solid solution. Thus, the lattice parameter (d) decreased due

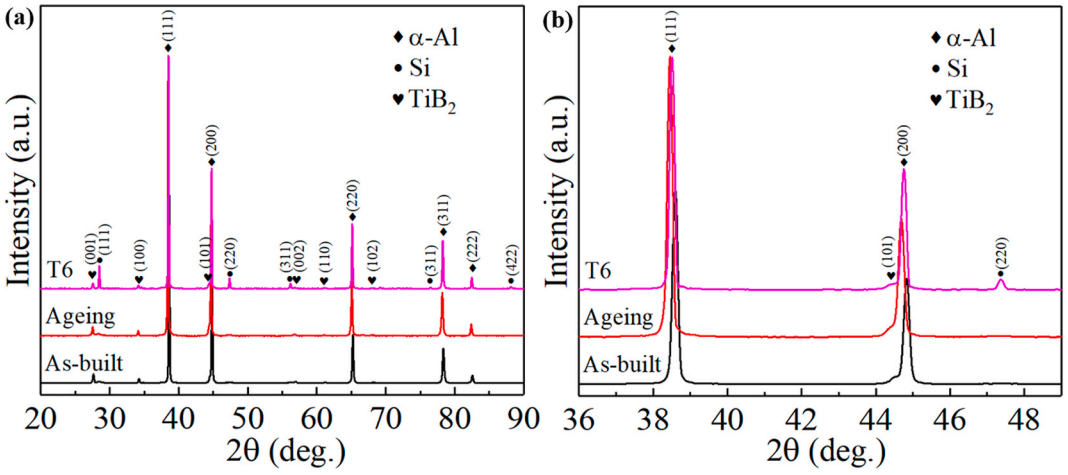

Fig. 3. XRD patterns of the SLMed TiB_2/Al–7Si–Cu–Mg alloy under as-built and heat-treated conditions: (a) $20° \leq 2\theta \leq 90°$, (b) $36° \leq 2\theta \leq 49°$.

to the small radius of Si dissolution into the Al matrix, so the peaks moved to the high angle for SLMed samples. When the phases containing Si element precipitated out during heat treatment, the lattice parameter increased, so the peaks moved to the low angle. Furthermore, after T6 treatment, the intensity of Si peaks increases obviously revealing that Si diffused out of the Al matrix due to the decrease of Si solid solubility.

3.2. Microstructure characterization

The EBSD results of longitudinal-section along the building direction (BD) of the SLMed TiB_2/Al–7Si–Cu–Mg alloy under as-built, direct ageing and T6 conditions are shown in Fig. 4. There are many reports on the grain analysis of SLMed Al–Si-based alloys revealing that the microstructures consist of coarse elongated grains with <001> fiber orientation texture [13,34–36]. However, for SLMed TiB_2/Al–7Si–Cu–Mg alloy, it can be seen from Fig. 4a and d that the as-built sample exhibits mostly equiaxed grain microstructure and the maximum texture intensity of {100} pole figure is only around 1.5 due to the heterogeneous nucleation effect of nano-TiB_2 particles (detail explanation can be found in our previous study [14,30]). According to the grain size distribution statistics of as-built sample in Fig. 4g, there are approximately 23% of the grains with grain size smaller than 1 μm, and the average grain size is around 2.23 μm. Besides, the aspect ratio (AR) of as-built sample is 2.06, which is much smaller than the AR (>4) of SLMed Al–Si-based alloy [30,36]. The above results suggest that the most fine equiaxed grains dominate the microstructure of as-built sample. After direct ageing at 150 °C for 12 h, the microstructural morphology and texture remained unchanged as shown in Fig. 4b and e. Fig. 4h shows the average grain size slightly increased by only 0.04 μm, and the AR of aged sample is 2.04 which is the same as the value of as-built sample. Fig. 4c revealed the obvious grain growth of the SLMed sample after T6 treatment. From Fig. 4i, the proportion of large grains (grain size > 5 μm) increased significantly, and the average grain size increased to 2.55 μm. Moreover, the AR of T6 treated sample reduced to 1.68 suggesting the equiaxed grains dominate the microstructure.

Fig. 5 presents the low magnification (a, c, e) and high magnification (b, d, f) SEM images featuring microstructures of the as-built sample (a, b) and the samples after direct ageing (c, d) and T6 treatment (e, f). The corresponding results of local chemical compositions of Points 1 to 3 and rectangular regions of 4 and 5 marked in Fig. 5 using EDS analysis are listed in Table 2. In the as-built sample (Fig. 5a and b), very fine equiaxed cell-like substructures are formed as a result of fast solidification during SLM process [30]. It can be seen that the primary α-Al cells are surrounded by cellular eutectic Si phase (diamond-like cubic structure from previous XRD analysis). After image processing and quantification of the SEM results, the mean diameter of cells is approximately 472 nm. The EDS analysis (Table 2) reveals the super solute of the main elements like Si, Cu and Mg in Al matrix. This result is consistent with the XRD analysis.

After direct ageing at 150 °C for 12 h, as shown in Fig. 5c and d, the

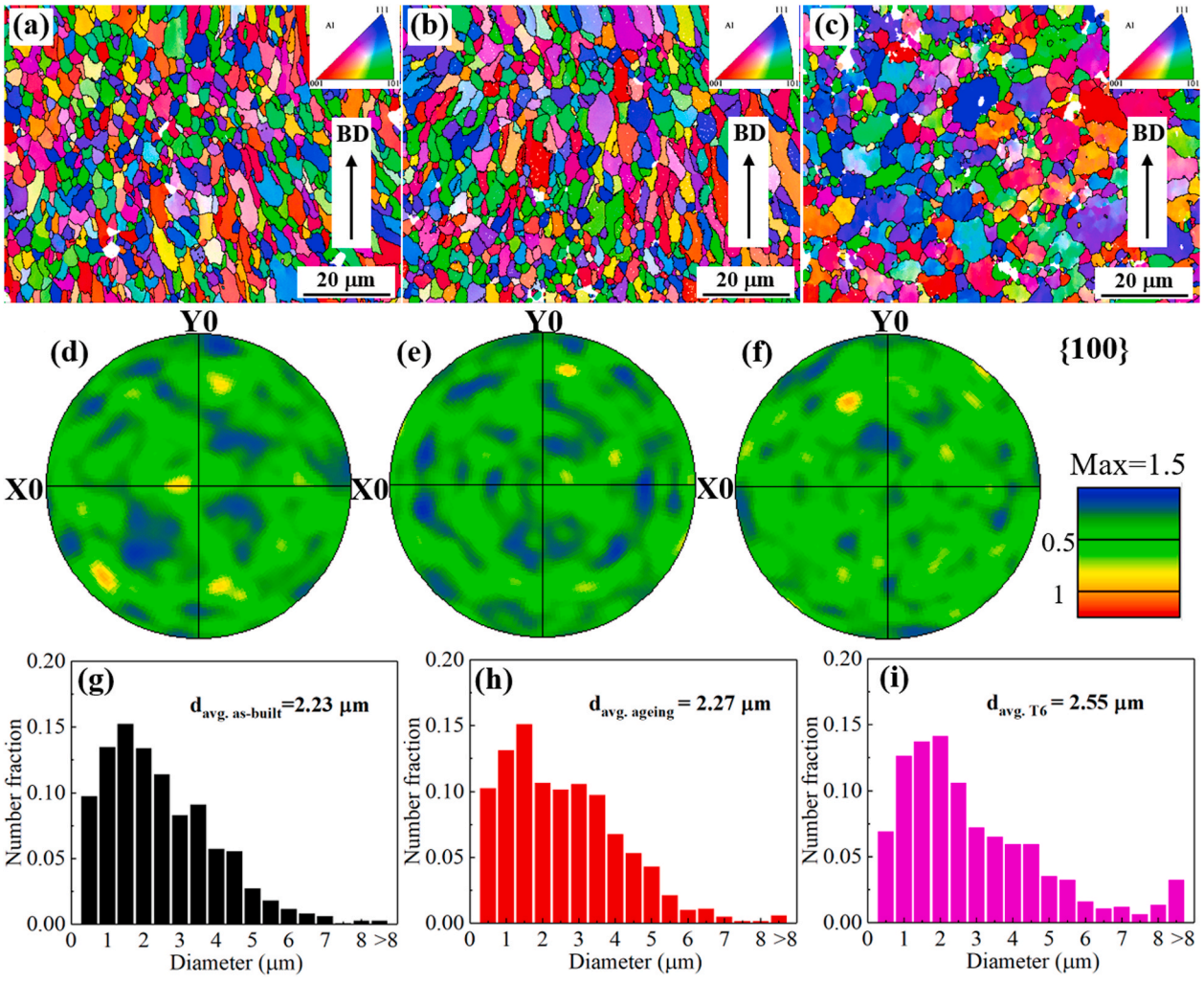

Fig. 4. (a-c) EBSD inverse pole figure (IPF) maps, (d-f) the corresponding pole figures and (g-i) the corresponding grain size distribution statistics of the SLMed TiB_2/Al–7Si–Cu–Mg alloy under different conditions: (a, d, g) as-built condition, (b, e, h) direct aged condition and (c, f, i) T6 treated condition.

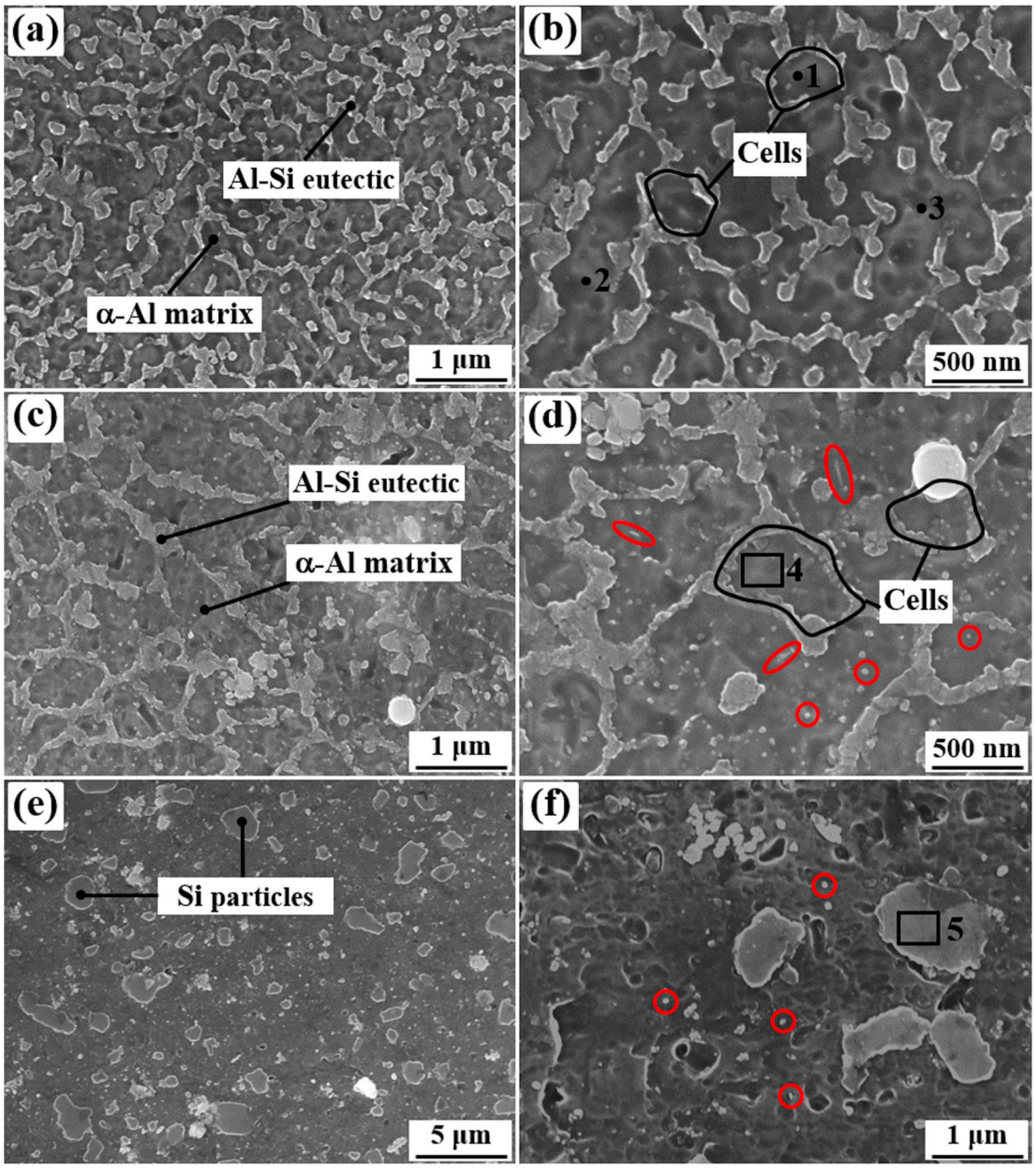

Fig. 5. SEM images of the SLMed TiB_2/Al–7Si–Cu–Mg under different treated conditions: (a, b) as-built, (c, d) direct ageing; (e, f) T6 treatment. Red circles in (d) and (f) indicate the new precipitates. (For interpretation of the references to colour in this figure legend, the reader is referred to the Web version of this article.)

Table 2
Local chemical compositions (wt. %) of Points 1 to 3 and rectangular regions of 4 and 5 shown in Fig. 5.

Number	Si	Cu	Mg
1	4.08	0.78	0.25
2	3.67	0.72	0.20
3	4.11	0.78	0.23
4	1.17	–	–
5	57.1	–	–

microstructure consisting of α-Al cells and eutectic Si boundaries remains unchanged. This suggests that the treatment at elevated temperature of 150 °C can not destroy the cellular eutectic Si sub-structures formed during rapid solidification. In addition, many new fine particles in spherical or short rod-like can be observed inside the α-Al cells (red arrows in Fig. 5d). The EDS analysis at rectangular regions of 4 shows that only 1.17 wt% Si is still in solution. Most of Si and all of Cu and Mg are dissipated to form the new precipitates. In the sample after T6 treatment (Fig. 5e and f), it can be seen that the precipitation of bulk Si particles become coarse and distribute homogenously in the α-Al matrix. The relatively coarsened particles of Si phase can reach a diameter above 1 μm. The results reveal that the high temperature (500 °C) solution treatment would destroy the fine microstructure due to the coarsening of Si phase. In the elevated temperature, the diffusion of elements, especially Si element, were accelerated to cause the redistribution of the elements.

To demonstrate what exactly happened in the sample during direct ageing treatment, TEM was applied to the SLMed TiB_2/Al–7Si–Cu–Mg sample under as-built and ageing treated conditions. Fig. 6 shows the bright-field (BF) TEM images that exhibit the microstructures of as-built sample. In the low magnification image (Fig. 6a), the cell substructure can be clearly seen as well. The obvious variation of diffraction contrast across the boundaries indicates the large misorientation between the

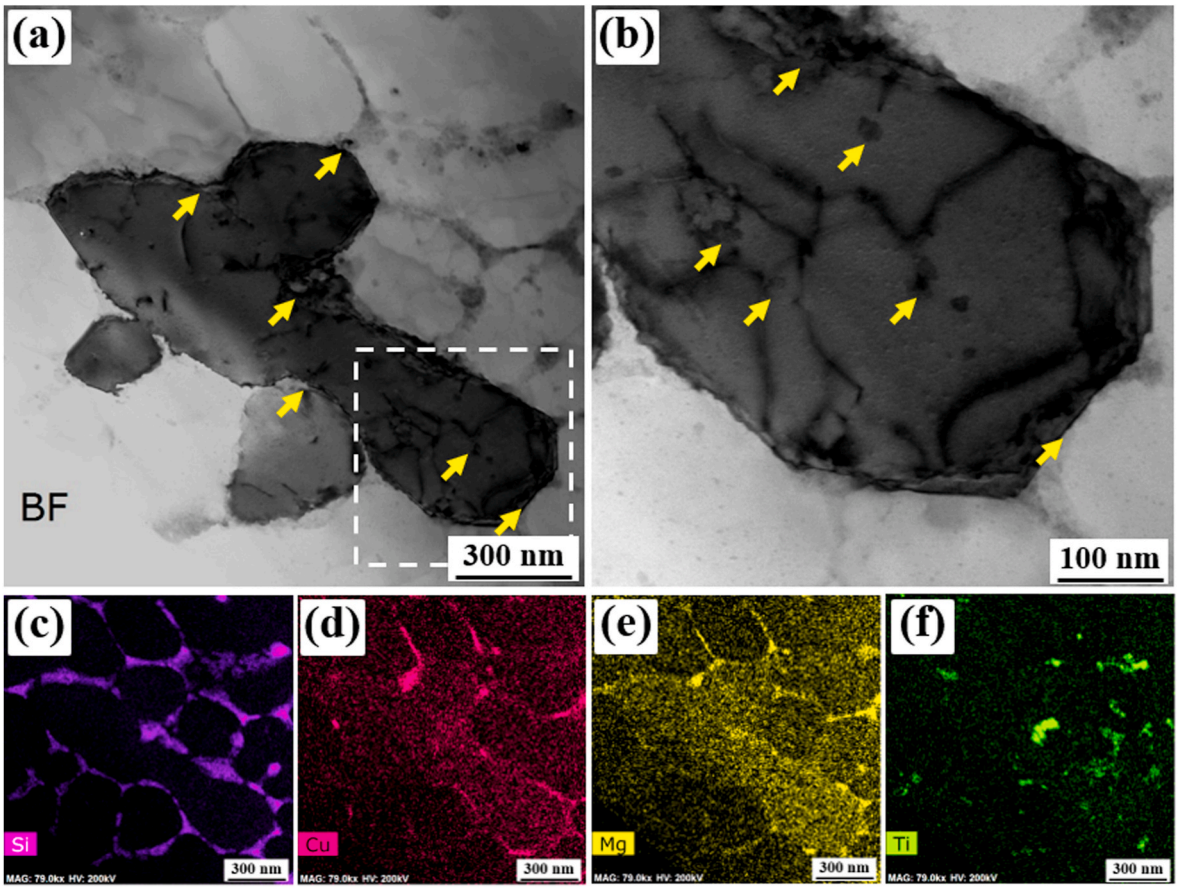

Fig. 6. (a) TEM BF images of the as-built TiB_2/Al–7Si–Cu–Mg sample, (b) zoom-in image of the white box area shown in (a), (c-f) corresponding EDX maps of Si, Cu, Mg and Ti elements to (a). Yellow arrows point to the nano-TiB_2 particles. (For interpretation of the references to colour in this figure legend, the reader is referred to the Web version of this article.)

neighboring structures. From the corresponding EDX maps in Fig. 6c-f, Si, Cu and Mg atoms clearly segregate along the cell boundaries. In addition, it can be clearly seen that the vast majority of the nano-TiB_2 particles (yellow arrows) are uniformly distributed in the sample, though some particles tend to distribute along the grain boundaries and cell boundaries. Furthermore, as shown in the high magnification image (Fig. 6b), there is some entangled dislocations inside the cell structures. The dislocations interact both with nano-TiB_2 particles and eutectic Si cell boundaries. Fig. 9 shows the results of quantitative characterization on dislocation density for SLMed alloy under as-built and heat-treated conditions by SRXRD. The dislocation density of as-built sample is 1.74×10^{14} m^{-2}, which is slightly higher than the results for SLMed AlSi10Mg alloy (1.4×10^{14} m^{-2}) in the literature [37]. The increase in the dislocation density may be explained by the mismatch of thermal expansion coefficient between α-Al matrix and TiB_2 particles.

Figs. 7 and 8 gives the bright-field (BF) TEM images of direct ageing treated TiB_2/Al–7Si–Cu–Mg sample. After the ageing treatment (Fig. 7a), the cell substructure with some tangled dislocations was not broken. The corresponding EDX maps in Fig. 7d–g showed that Si, Cu and Mg atoms still segregated along the cell boundaries. In the high magnification image (Fig. 7b) of white square area of Fig. 7a, many dot-like nano-precipitates can be observed inside the cells. In addition, some acicular precipitates were also distinguished. As shown in Fig. 7c, the selected area electron diffraction (SAED) image of red circled area in Fig. 7b revealed that the nano-scale precipitates are Al_2Cu (θ′) and Si phases. Fig. 8 shows the details inside the cells, and there are some needles-like particles, as presented by yellow arrows in Fig. 8a. These needle-like precipitates have a length of ~200 nm, and width of ~10 nm. They are identified to be pure Si particles from the elemental mapping in Fig. 8b. These precipitates are aligned parallel or perpendicular to each other. A representative HRTEM micrograph along with the FFT for the needle-like precipitate is presented in Fig. 8c. After ageing at 150 °C, there are partial dislocations annihilation by recovery, and the dislocation density slightly reduced to 1.28×10^{14} m^{-2}. While after T6 treatment, the dislocation density reduced to only 0.23×10^{14} m^{-2}.

3.3. Mechanical properties

Fig. 10a presents the engineering tensile stress-strain curves at room temperature of the SLMed TiB_2/Al–7Si–Cu–Mg samples under as-built and after direct ageing or T6 heat-treated conditions. The corresponding comparisons of yield strength (YS), ultimate tensile stress (UTS) and elongation (El) are summarized in Table 3. The results indicate that the as-built TiB_2/Al–7Si–Cu–Mg samples exhibit a yield strength of 297.2 MPa. The flow stress increases at a relatively high strain hardening rate and then reaches the ultimate tensile strength of 474.6 MPa. The tensile elongation is approximately 13.4%. After direct ageing treatment, the specimen exhibits a higher strength and lower ductility. YS markedly increases by 35%–400.7 MPa and UTS increases by 9%–517.9 MPa, and meanwhile, the El decreases to 9.6%. While for T6 treatment, the method commonly used to enhance strength in conventional Al alloys, a large decrease in both strength and ductility can be observed. It can be seen that YS and UTS decrease approximately by 16%–248.7 MPa and by 30%–330.2 MPa respectively, and El decreases to 9.9%. Fig. 10b compares the tensile properties of our results with those published in recent reports. It can be seen that SLMed TiB_2/Al–7Si–Cu–Mg samples show superior tensile performance, especially after direct ageing

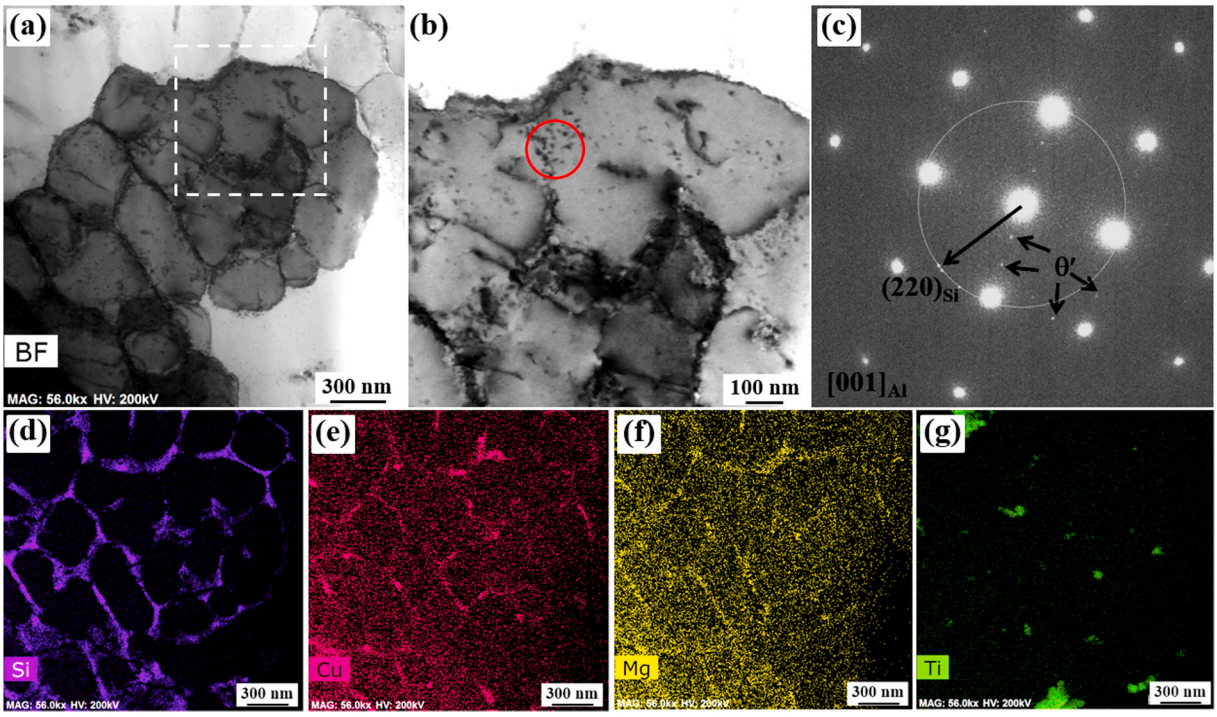

Fig. 7. (a) TEM BF images of the direct ageing treated TiB_2/Al–7Si–Cu–Mg, (b) zoom-in image of the white box area shown in (a), (c) the corresponding SAED image of red circle area in (b), (d-g) corresponding EDX maps of Si, Cu, Mg and Ti elements to (a). (For interpretation of the references to colour in this figure legend, the reader is referred to the Web version of this article.)

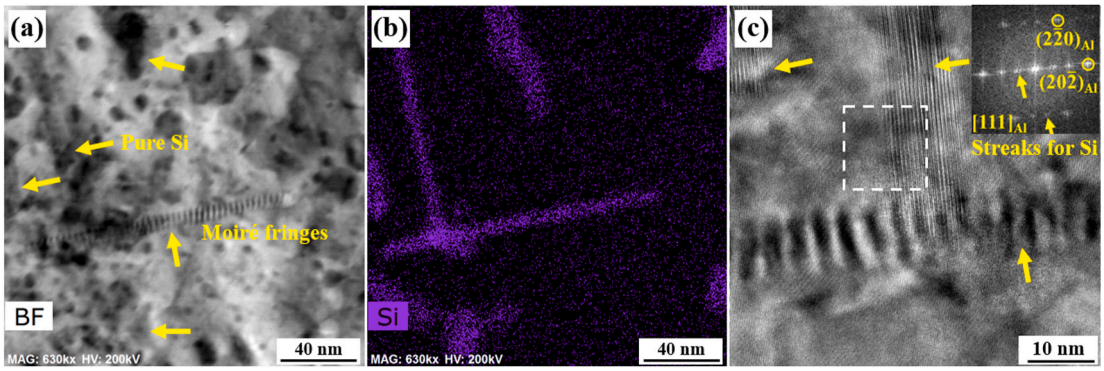

Fig. 8. (a) TEM BF images of the direct ageing treated TiB_2/Al–7Si–Cu–Mg, (b) corresponding EDX maps of Si to (a), (c) HRTEM of precipitates in (a), inset is the corresponding SAED image of white square area in (c).

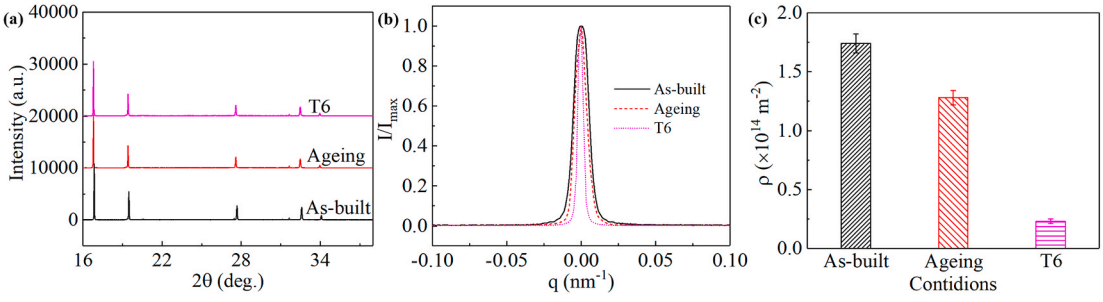

Fig. 9. Quantitative characterization on dislocation density for SLMed TiB_2/Al–7Si–Cu–Mg alloy under as-built and heat-treated conditions by SRXRD. (a) The diffraction peaks of the samples, (b) normalized peaks for the samples, (c) dislocation density for three samples. The dislocation density is taken as the average of (111), (200), (220) and (311) peaks.

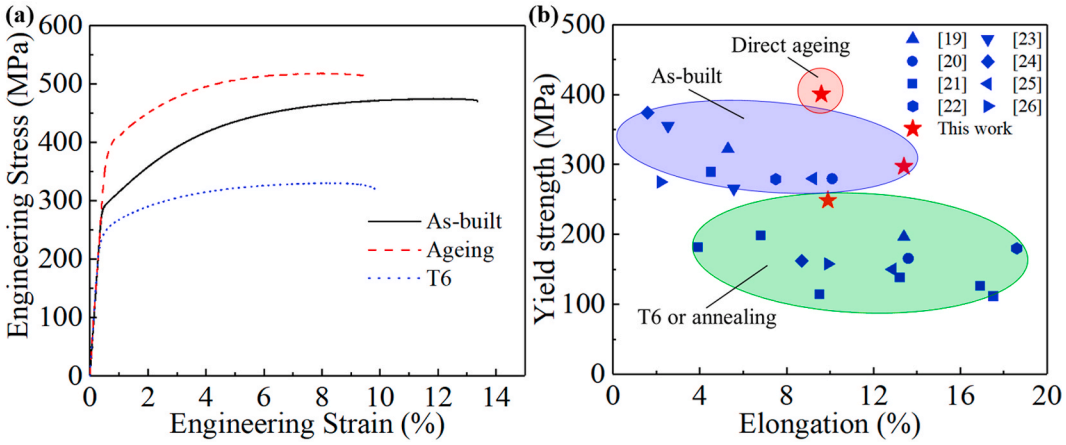

Fig. 10. (a) The tensile stress-strain curves of the SLMed TiB_2/Al–7Si–Cu–Mg alloy under as-built and heat-treated conditions; (b) comparison of tensile properties of our work and other reports.

Table 3
Tensile properties of the SLMed TiB_2/Al–7Si–Cu–Mg alloy samples under as-built and after heat-treated conditions.

State	YS (MPa)	UTS (MPa)	El (%)
As-built	297.2 ± 0.2	474.6 ± 1.8	13.4 ± 0.5
Ageing	400.7 ± 1.2	517.9 ± 1.4	9.6 ± 0.3
T6	248.7 ± 0.8	330.2 ± 1.0	9.9 ± 0.6

treatment.

The fractographic analyses after tensile testing of the SLMed specimens under different conditions are shown in Fig. 11. A vast number of equiaxed dimples can be clearly seen over the entire fracture surface in all samples. The results indicate micro-void coalescence and deformation by slip, and reveal the occurrence of ductile fracture rather than brittle fracture. It should be noted that, in the as-built specimen (Fig. 11a–c), the dimples are deep and fine. The average dimple size is around 500 nm close to the size of α-Al cells. Besides, a few pore defects formed during SLM process can be observed on the fracture surface. The corresponding magnified image of a pore in Fig. 9c revealed that the cracks initiated at the cell boundaries that contain brittle Si phases. The fracture characteristics of samples after direct ageing (Fig. 11d) showed almost the same results of as-built samples. The corresponding chemical distribution of Si element indicates that the cracks initiate and propagate along the Si boundaries until complete separation occurs. After T6 treatment, as seen in the dimpled surface in Fig. 11e, the fracture features coarsen. Voids nucleate at the large Si particles by de-cohesion then void coalescence occurs. The breakage of Si particles occurs and cracks initiate along the breakage. The chemical distribution of the main elements in the materials (mapped in Fig. 11f) confirms the scenario of the breakage of large Si particles as well as the microstructural coarsening.

4. Discussion

4.1. Microstructure development with heat treatment

The present work set out to study the crystallographic features and microstructures of SLMed TiB_2/Al–7Si–Cu–Mg samples that had been post heat treated at different conditions, to elucidate the microstructure development during heat treatment. First and foremost, we need to have a good understanding of the initial structure at as-built condition. The hierarchical microstructures including grains, cell-substructures, precipitates and dislocations, are typical for SLMed samples. For the nano-TiB_2 decorated Al–Si alloy, as depicted in our previous work [14,30], the very fine primary α-Al cells firstly solidified based on the TiB_2 particles (effective nucleating agent for Al). Subsequently, the continuous networks of eutectic Si began to form at the end of the solidification process. Due to the rapid solidification of SLM, the supersaturation of Si, Cu and Mg elements is obtained in Al matrix. Besides, our results reveal that there is no obvious nano-scale precipitates like Si or Mg_2Si in the as-built sample. Additionally, some entangled dislocations developed inside the cells.

As for the direct ageing treatment, the above analysis of the present study reveals that there is almost no change in the microstructure including grains and cell structures. The EBSD results (Fig. 4) indicate that the microstructural features in grain level (e.g. grain size, aspect ratio, etc.) remain unchanged. The SEM images exhibit that the cell structures inside the α-Al grains stay the as-built look (Fig. 5). One of the new findings was the observation of nano-sized Al_2Cu and Si phases within the cells. Additionally, the precipitates prefer to be distributed close to the tangled distributions and cell boundaries. The observed fine new precipitates within the α-Al matrix also indicate that the existence of Si, Cu and Mg supersaturation in the α-Al matrix of the as-built samples.

After the conventional T6 treatment, the fine microstructure, especially the cell sub-structure, caused by rapid solidification during SLM is completely destroyed. The EBSD analysis of the present study shows a slight growth of the α-Al grains during the treatment. The mean spacing of the high angle grain boundaries (HAGBs) was found to increase slightly. Considering the sub-structures and tangled dislocations in the as-built samples, the microstructure evolution is likely due to the recovery process, meaning the occurrence of annihilation of the dislocations. Besides, the intriguing fine Si substructure within the equiaxed α-Al grains was barely observed due to the treatment at high temperature (500 °C). The fine eutectic Si structures dissolve firstly and then coarsen during the solution heat treatment.

Based on the above discussion, the microstructure development in SLMed TiB_2/Al–7Si–Cu–Mg sample during post heat treatment can be schematically illustrated, as depicted in Fig. 12. As shown in Fig. 12a, the as-built samples reveal the fine equiaxed α-Al grains. The equiaxed α-Al grains consist of several cells (firstly solid) surrounded by eutectic Si phases (Si-rich liquid with a low melting point, finally solid). Tangled array of dislocations developed inside the cells due to the rapid solidification during SLM process. After direct ageing treatment (Fig. 12b), the fine grains and cell structure remain unchanged. The fine Al_2Cu and Si phases precipitate inside the α-Al cells around the dislocations or cell boundaries. After T6 treatment (Fig. 12c), the grains grow up, the cell structures disappear and the fine eutectic Si phases become coarser.

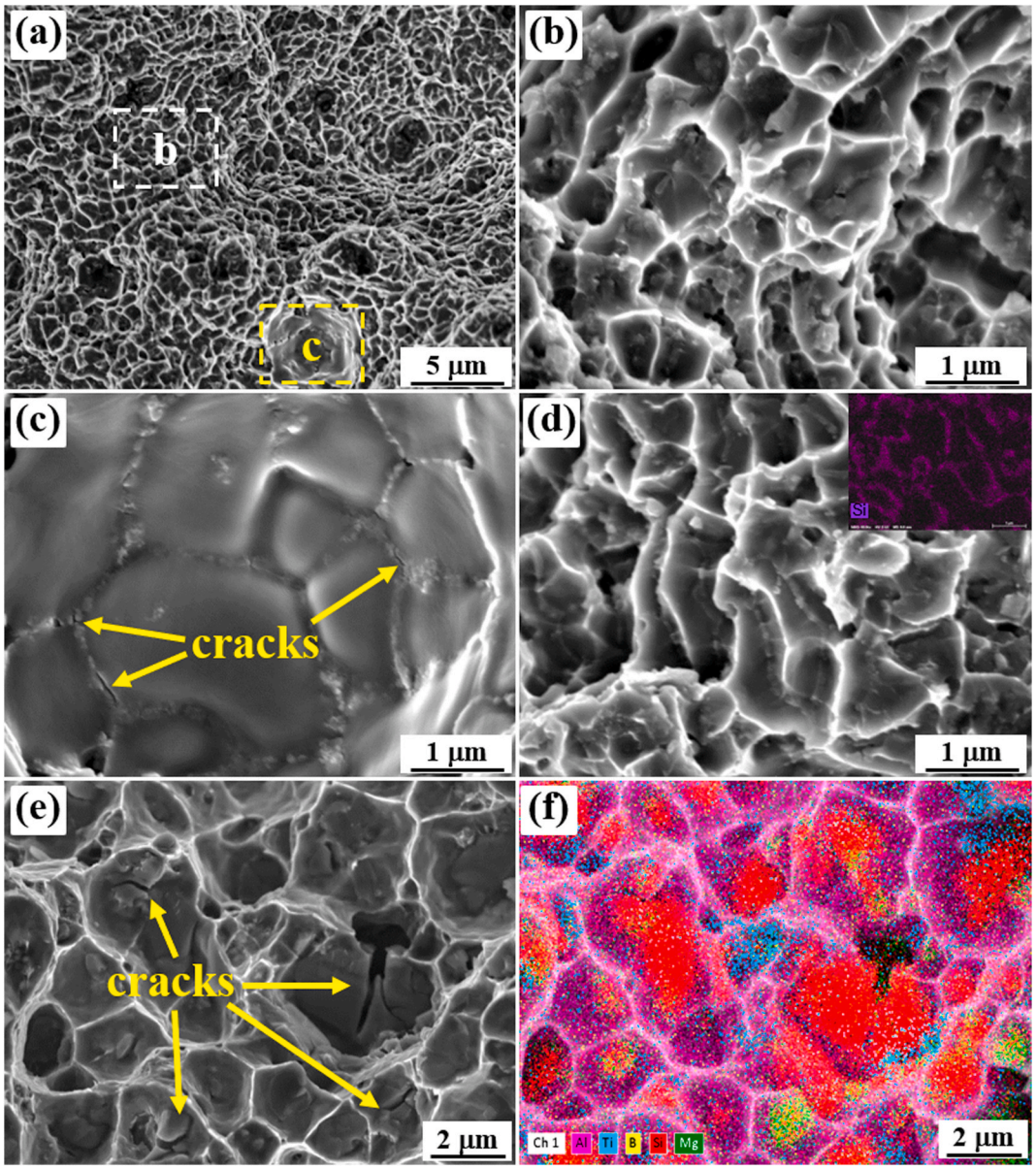

Fig. 11. The SEM fracture surfaces of SLMed TiB_2/Al–7Si–Cu–Mg samples under different conditions: (a) as-built, (b) the zoom-in image of the white box area shown in (a), (c) the zoom-in image of the yellow box area shown in (a); (d) direct ageing, inset is the corresponding EDX mapping of Si element; (e) T6 treatment, (f) the corresponding EDX mapping of Al, Ti and Si elements of (e). (For interpretation of the references to colour in this figure legend, the reader is referred to the Web version of this article.)

4.2. Strengthening mechanisms associated with microstructure

The potential strengthening mechanisms of the SLM TiB_2/Al–7Si–Cu–Mg alloy under different treated conditions are discussed below. According to the conventional strengthening mechanisms, there are several contributions to the yield strength (YS) and the contribution to strength can be described as follows:

$$YS = \sigma_0 + \sigma_B + \sigma_{SS} + \sigma_{dis} + \sigma_P + \sigma_D \quad (2)$$

where σ_0 is the internal lattice friction stress for pure Al (base strength of pore Al), σ_B represents the strength increment of grain/cell boundary strengthening (Hall-Petch effect), σ_{SS} represents the strength increment of solid solution strengthening by solutes like Si, Cu and Mg, σ_{dis} represents the strength increment of dislocation strengthening by the pre-existing dislocations, σ_P represents the strength increment of precipitation strengthening by nano-scale new phases, σ_D represents the strength increment of dispersoid strengthening mainly from TiB_2 particles. Qualitative estimates of the contribution of each mechanism in the SLMed TiB_2/Al–7Si–Mg–Cu materials are described below.

During post heat treatment, the value of base strength is considered constant. Besides, the distribution of nano-TiB_2 particles was unchanged, and thus, the contribution by the dispersion strengthening can be neglected in all states. Therefore, the discussion will focus on the other four contributions.

The contribution by the grain/cell boundary strengthening can be described by the analogous Hall-Petch equation [23,38]:

$$\sigma_B = kd^{-1/2} \quad (3)$$

where k is the Hall-Petch coefficient (50 MPa $\mu m^{1/2}$ for Al [14]) and d is the average grain/cell diameter. As for the as-built and direct ageing samples, the cell boundaries inside the grains can also impede the dislocation movement during deformation in SLMed Al–Si alloys, as

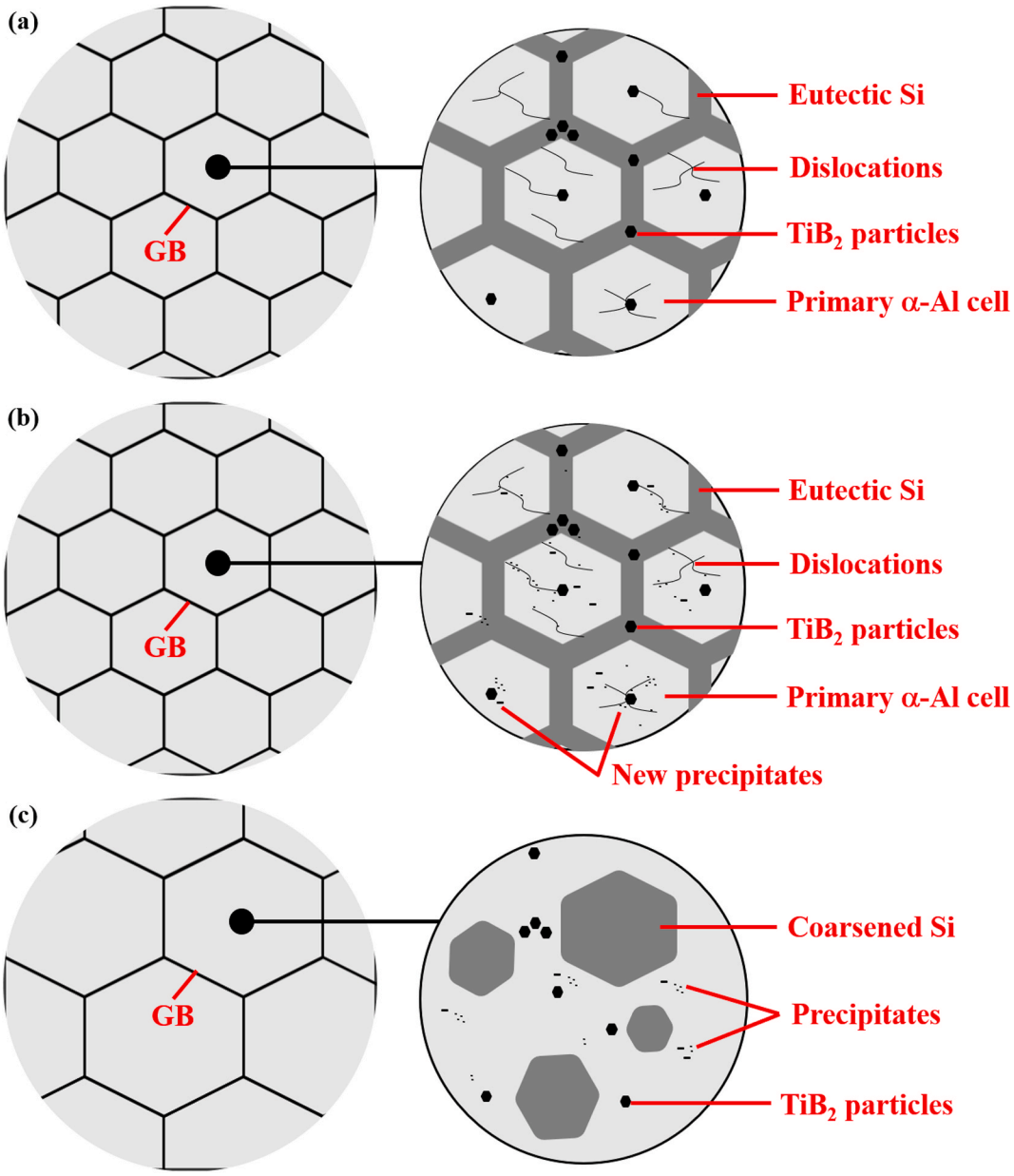

Fig. 12. Schematic showing the development in microstructure of SLMed TiB_2/Al–7Si–Cu–Mg sample: (a) as-built, (b) direct ageing and (c) T6 treatment.

observed by in-situ TEM [35]. Thus, the value of d is chosen as the width of the cellular eutectic Si sub-structures (0.472 μm), which is extracted from the SEM characterization using Image J software. While the cell structures disappear after T6 treatment, so the value of d is chosen as the grain size from EBSD results (2.55 μm). Consequently, the contributions of grain/cell boundary strengthening to YS are calculated to be 72.8 MPa for as-built and direct ageing, and 31.3 MPa for T6 treatment.

Due to the fast cooling rate during SLM process, a supersaturation of solutes including Si, Cu and Mg is achieved, leading to a considerable amount of solid solution strengthening. The contribution of solid solution strengthening is given by:

$$\sigma_{SS} = k_{Si}(C_{\alpha}^{Si})^{m} + k_{Cu}(C_{\alpha}^{Cu})^{m} + k_{Mg}(C_{\alpha}^{Mg})^{m} \quad (4)$$

where k_{Si} is 11 MPa/wt.%, k_{Cu} is 13.8 MPa/wt.%, k_{Mg} is 18.6 MPa/wt.% and m is 1 [23,39]. From the EDS results of as-built samples (Table 2), we calculated the mean values of points 1, 2 and 3 inside the cells, and around 3.95 wt% of the Si, 0.76 wt% of the Cu and 0.23 wt% of the Mg are in solution. Thus, the contributions to the YS by solid solution from Si, Cu and Mg can be determined as 43.5 MPa, 10.5 MPa and 6.1 MPa, respectively. The total contribution is 60.1 MPa. As for the directly aged samples, there will be little Cu and Mg still in solution due to its fast diffusion rate, while some residual Si (1.17 wt%) still in solution. Thus, under ageing condition, the contribution to the YS by solid solution from Si can be determined as 12.7 MPa. As for T6 treated samples, there are almost none solid solutions in the Al matrix, so the contribution to the YS by the solid solution can be neglected.

The above results confirmed that pre-existing entangled dislocations are formed in the as-built condition of SLMed Al due to the internal stresses. Thus, there is the contribution from dislocations in as-built sample, and its contribution can be calculated as:

$$\sigma_{dis} = \beta M G b \sqrt{\rho_{dis}}$$

where β is a material constant (~0.16 for Al), M is the Taylor factor (3.06 for FCC crystals), G and b are the shear modulus (~26.5 GPa) and Burgers vector (0.286 nm) of Al, and ρ_{dis} is the dislocation density (Fig. 9). Thus, the contribution of dislocations to the YS of as-built

sample can be estimated as 48.9 MPa. During ageing at 150 °C, there are partial dislocations annihilation by recovery, so the contribution reduced to 42.0 MPa. While during solution treatment of T6, the dislocations were annihilated and rearranged inside the cells leading to a complete recovery. Then, during quenching of T6, dislocations can also form and the contribution to YS is calculated as 17.8 MPa. Thus, for T6 treated samples, the contribution of dislocations to the YS is 17.8 MPa.

As for the precipitation strengthening, the new nano-scale phases like Al_2Cu, Si and Mg_2Si formed during post heat treatment could contribute to the yield strength. Yang, Wang and Hadadzadeh et al. have investigated the contribution from precipitate strengthening of SLMed Al–Si-(Cu)–Mg alloy during post-heat treatment [39–41]. However, it is difficult to get the critical particle sizes at the shearable to non-shearable transition. There are some reports which found Si particles are non-shearable and calculated the precipitation strengthening through Orowan mechanism [37]. The contribution of precipitates is given by:

$$\sigma_P = \frac{\phi G b}{d_P}\left(\frac{6V_P}{\pi}\right)^{1/3}$$

where ϕ is a material constant, G is the shear modulus of Al, b is the Burgers vector of Al, d_P is the average diameter of precipitate particles, and V_P is the volume fraction of the particles. It is difficult to get the values of average diameter and volume fraction. Thus, the contribution of Si precipitates can not be estimated accurately, not to mention the competitions from Al_2Cu and Mg_2Si precipitates. Therefore, the contribution of precipitates to YS for direct ageing and T6 treated samples will be estimated using the compensation method.

After direct ageing, the increment of yield strength is significant ($\Delta YS = 103.5\,MPa$). The above calculated results give the respective strengthening contributions: the changed contribution of grain/cell boundary strengthening can be neglected; the changed contribution of dislocation strengthening is −6.9 MPa; and the changed contribution of solid solution strengthening is −47.4 MPa. As a result, the contribution of precipitates can be estimated as 157.8 MPa. It is evident that the precipitation strengthening has the most significant effect on the noticeable increase of yield strength of samples after direct ageing treatment. The result is consistent with the previous works [39,40].

It is particularly interesting that the traditional T6 heat treatment significantly reduced the strength ($\Delta YS = -48.5\,MPa$). The possible reasons can be attributed to the following aspects. Firstly, the destruction of eutectic Si cell structure leads to the decrease of contribution of boundary strengthening ($\Delta\sigma_B = -41.5$ MPa). In the as-built sample, the Si sub-boundaries inside the grains can also impede the dislocation movement during deformation. After T6 treatment, the cell boundaries are broken and the cell boundary strengthening disappears. Thus, only grain boundary strengthening contributions to the YS. Secondly, the reduced solid solution hardening by solutes decreases contributes to lower strength ($\Delta\sigma_{SS} = -60.1$ MPa). Thirdly, the reduction of dislocation density leads to the decrease of contribution of σ_{dis} ($\Delta\sigma_{dis} = -31.1$ MPa). Last, but not least, the precipitation strengthening by Si, Mg_2Si and Al_2Cu particles contribute to YS ($\Delta\sigma_P = 84.2$ MPa). As for Si phases, the coarsened Si particles can still be the resistance to dislocation motion. Besides, the new Mg_2Si and Al_2Cu precipitates formed during T6 treatment provide significant contributions to YS through Orowan strengthening.

5. Conclusions

The present study investigated the effects of heat treatment on the microstructure and mechanical properties of TiB_2/Al–7Si–Cu–Mg sample fabricated by SLM. The results help to understand the microstructure development and the related mechanical properties, especially the strength. The following conclusions can be drawn:

(1) The as-built TiB_2/Al–7Si–Cu–Mg sample exhibits fine equiaxed grain structures without preferred crystallographic texture due to the high cooling rate of SLM and the addition of nano-TiB_2 particles. Nano-scale eutectic Si cells are present within the equiaxed grains. There are dislocation tangles around the nano-TiB_2 particles or cell boundaries inside the cells. No obvious precipitates are observed within the matrix.

(2) In the TiB_2/Al–7Si–Cu–Mg sample that was directly ageing treated, the grain and cell structures remain almost unchanged. New phases, Al_2Cu, Mg_2Si, and Si particles, are found to precipitate around the dislocations within the cells. While after T6 treatment, the fine grains grow up and the eutectic Si phases coarse leading to the broken of cell structures.

(3) The as-built TiB_2/Al–7Si–Cu–Mg samples show high tensile strength and ductility (yield strength: 297.2 MPa, ultimate tensile strength: 474.6 MPa, elongation: 13.4%). After ageing, the new nano-scale precipitates enhance the yield strength by ~35%. While the broken of eutectic Si sub-structure during T6 leads to the decrease of yield strength by ~16%. The present result provides an important insight into the control of post heat treatment of the TiB_2/Al–7Si–Cu–Mg samples fabricated by SLM.

Data availability

The raw/processed data required to reproduce these findings cannot be shared at this time as the data also forms part of an ongoing study.

CRediT authorship contribution statement

Y.K. Xiao: Investigation, Validation, Writing - original draft. **Q. Yang:** Investigation, Resources, Formal analysis, Writing - review & editing. **Z.Y. Bian:** Data curation, Formal analysis, Writing - review & editing. **H. Chen:** Data curation, Formal analysis, Writing - review & editing. **Y. Wu:** Conceptualization, Resources, Formal analysis, Writing - review & editing. **Q. Lian:** Data curation, Formal analysis, Writing - review & editing. **Z. Chen:** Conceptualization, Funding acquisition, Formal analysis, Writing - review & editing. **H.W. Wang:** Resources, Supervision, Writing - review & editing.

Declaration of competing interest

The authors declare that they have no known competing financial interests or personal relationships that could have appeared to influence the work reported in this paper.

Acknowledgement

This work was supported by the National Key Research and Development Program of China (Grant No. 2016YFB1100100).

References

[1] T. DebRoy, T. Mukherjee, J.O. Milewski, J.W. Elmer, B. Ribic, J.J. Blecher, W. Zhang, Scientific, technological and economic issues in metal printing and their solutions, Nat. Mater. 18 (2019) 1026–1032, https://doi.org/10.1038/s41563-019-0408-2.

[2] D. Herzog, V. Seyda, E. Wycisk, C. Emmelmann, Additive manufacturing of metals, Acta Mater. 117 (2016) 371–392, https://doi.org/10.1016/j.actamat.2016.07.019.

[3] T. DebRoy, H.L. Wei, J.S. Zuback, T. Mukherjee, J.W. Elmer, J.O. Milewski, A. M. Beese, A. Wilson-Heid, A. De, W. Zhang, Additive manufacturing of metallic components – process, structure and properties, Prog. Mater. Sci. 92 (2018) 112–224, https://doi.org/10.1016/j.pmatsci.2017.10.001.

[4] L. Thijs, F. Verhaeghe, T. Craeghs, J.V. Humbeeck, J.-P. Kruth, A study of the microstructural evolution during selective laser melting of Ti–6Al–4V, Acta Mater. 58 (2010) 3303–3312, https://doi.org/10.1016/j.actamat.2010.02.004.

[5] W. Xu, M. Brandt, S. Sun, J. Elambasseril, Q. Liu, K. Latham, K. Xia, M. Qian, Additive manufacturing of strong and ductile Ti–6Al–4V by selective laser melting via in situ martensite decomposition, Acta Mater. 85 (2015) 74–84, https://doi.org/10.1016/j.actamat.2014.11.028.

[6] M. Simonelli, Y.Y. Tse, C. Tuck, Effect of the build orientation on the mechanical properties and fracture modes of SLM Ti–6Al–4V, Mater. Sci. Eng., A 616 (2014) 1–11, https://doi.org/10.1016/j.msea.2014.07.086.
[7] X. Wang, J.A. Muñiz-Lerma, O. Sanchez-Mata, M. Attarian Shandiz, N. Brodusch, R. Gauvin, M. Brochu, Characterization of single crystalline austenitic stainless steel thin struts processed by laser powder bed fusion, Scripta Mater. 163 (2019) 51–56, https://doi.org/10.1016/j.scriptamat.2018.12.032.
[8] M. Mukherjee, Effect of build geometry and orientation on microstructure and properties of additively manufactured 316L stainless steel by laser metal deposition, Materialia 7 (2019) 100359, https://doi.org/10.1016/j.mtla.2019.100359.
[9] N.P. Lavery, J. Cherry, S. Mehmood, H. Davies, B. Girling, E. Sackett, S.G.R. Brown, J. Sienz, Effects of hot isostatic pressing on the elastic modulus and tensile properties of 316L parts made by powder bed laser fusion, Mater. Sci. Eng., A 693 (2017) 186–213, https://doi.org/10.1016/j.msea.2017.03.100.
[10] E. Chauvet, P. Kontis, E.A. Jägle, B. Gault, D. Raabe, C. Tassin, J.-J. Blandin, R. Dendievel, B. Vayre, S. Abed, G. Martin, Hot cracking mechanism affecting a non-weldable Ni-based superalloy produced by selective electron Beam Melting, Acta Mater. 142 (2018) 82–94, https://doi.org/10.1016/j.actamat.2017.09.047.
[11] N.J. Harrison, I. Todd, K. Mumtaz, Reduction of micro-cracking in nickel superalloys processed by Selective Laser Melting: a fundamental alloy design approach, Acta Mater. 94 (2015) 59–68, https://doi.org/10.1016/j.actamat.2015.04.035.
[12] K. Kunze, T. Etter, J. Grässlin, V. Shklover, Texture, anisotropy in microstructure and mechanical properties of IN738LC alloy processed by selective laser melting (SLM), Mater. Sci. Eng., A 620 (2015) 213–222, https://doi.org/10.1016/j.msea.2014.10.003.
[13] L. Thijs, K. Kempen, J.-P. Kruth, J. Van Humbeeck, Fine-structured aluminium products with controllable texture by selective laser melting of pre-alloyed AlSi10Mg powder, Acta Mater. 61 (2013) 1809–1819, https://doi.org/10.1016/j.actamat.2012.11.052.
[14] X.P. Li, G. Ji, Z. Chen, A. Addad, Y. Wu, H.W. Wang, J. Vleugels, J. Van Humbeeck, J.P. Kruth, Selective laser melting of nano-TiB2 decorated AlSi10Mg alloy with high fracture strength and ductility, Acta Mater. 129 (2017) 183–193, https://doi.org/10.1016/j.actamat.2017.02.062.
[15] H. Rao, S. Giet, K. Yang, X. Wu, C.H.J. Davies, The influence of processing parameters on aluminium alloy A357 manufactured by Selective Laser Melting, Mater. Des. 109 (2016) 334–346, https://doi.org/10.1016/j.matdes.2016.07.009.
[16] K. Kempen, L. Thijs, J. Van Humbeeck, J.-P. Kruth, Processing AlSi10Mg by selective laser melting: parameter optimisation and material characterisation, Mater. Sci. Technol. 31 (2015) 917–923, https://doi.org/10.1179/1743284714Y.0000000702.
[17] E.O. Olakanmi, Selective laser sintering/melting (SLS/SLM) of pure Al, Al–Mg, and Al–Si powders: effect of processing conditions and powder properties, J. Mater. Process. Technol. 213 (2013) 1387–1405, https://doi.org/10.1016/j.jmatprotec.2013.03.009.
[18] N.T. Aboulkhair, 3D printing of Aluminium alloys: additive Manufacturing of Aluminium alloys using selective laser melting, Prog. Mater. Sci. 106 (2019) 100578.
[19] K.G. Prashanth, S. Scudino, J. Eckert, Defining the tensile properties of Al-12Si parts produced by selective laser melting, Acta Mater. 126 (2017) 25–35, https://doi.org/10.1016/j.actamat.2016.12.044.
[20] J.H. Rao, Y. Zhang, X. Fang, Y. Chen, X. Wu, C.H.J. Davies, The origins for tensile properties of selective laser melted aluminium alloy A357, Additive Manufacturing 17 (2017) 113–122, https://doi.org/10.1016/j.addma.2017.08.007.
[21] W. Li, S. Li, J. Liu, A. Zhang, Y. Zhou, Q. Wei, C. Yan, Y. Shi, Effect of heat treatment on AlSi10Mg alloy fabricated by selective laser melting: microstructure evolution, mechanical properties and fracture mechanism, Mater. Sci. Eng., A 663 (2016) 116–125, https://doi.org/10.1016/j.msea.2016.03.088.
[22] Y. Bai, Y. Yang, Z. Xiao, M. Zhang, D. Wang, Process optimization and mechanical property evolution of AlSiMg0.75 by selective laser melting, Mater. Des. 140 (2018) 257–266, https://doi.org/10.1016/j.matdes.2017.11.045.
[23] K. Ma, H. Wen, T. Hu, T.D. Topping, D. Isheim, D.N. Seidman, E.J. Lavernia, J. M. Schoenung, Mechanical behavior and strengthening mechanisms in ultrafine grain precipitation-strengthened aluminum alloy, Acta Mater. 62 (2014) 141–155, https://doi.org/10.1016/j.actamat.2013.09.042.
[24] M. Wang, B. Song, Q. Wei, Y. Zhang, Y. Shi, Effects of annealing on the microstructure and mechanical properties of selective laser melted AlSi7Mg alloy, Mater. Sci. Eng., A 739 (2019) 463–472, https://doi.org/10.1016/j.msea.2018.10.047.
[25] M. Fousová, D. Dvorský, A. Michalcová, D. Vojtěch, Changes in the microstructure and mechanical properties of additively manufactured AlSi10Mg alloy after exposure to elevated temperatures, Mater. Char. 137 (2018) 119–126, https://doi.org/10.1016/j.matchar.2018.01.028.
[26] N. Takata, H. Kodaira, K. Sekizawa, A. Suzuki, M. Kobashi, Change in microstructure of selectively laser melted AlSi10Mg alloy with heat treatments, Mater. Sci. Eng., A 704 (2017) 218–228, https://doi.org/10.1016/j.msea.2017.08.029.
[27] A.H. Maamoun, M. Elbestawi, G.K. Dosbaeva, S.C. Veldhuis, Thermal post-processing of AlSi10Mg parts produced by Selective Laser Melting using recycled powder, Additive Manufacturing 21 (2018) 234–247, https://doi.org/10.1016/j.addma.2018.03.014.
[28] P. Yang, M.A. Rodriguez, L.A. Deibler, B.H. Jared, J. Griego, A. Kilgo, A. Allen, D. K. Stefan, Effect of thermal annealing on microstructure evolution and mechanical behavior of an additive manufactured AlSi10Mg part, J. Mater. Res. 33 (2018) 1701–1712, https://doi.org/10.1557/jmr.2018.82.
[29] N.T. Aboulkhair, I. Maskery, C. Tuck, I. Ashcroft, N.M. Everitt, The microstructure and mechanical properties of selectively laser melted AlSi10Mg: the effect of a conventional T6-like heat treatment, Mater. Sci. Eng., A 667 (2016) 139–146, https://doi.org/10.1016/j.msea.2016.04.092.
[30] Y. Xiao, Z.Y. Bian, Y. Wu, G. Ji, Y.Q. Li, M.J. Li, Q. Lian, Z. Chen, A. Addad, H. W. Wang, Effect of nano-TiB2 particles on the anisotropy in an AlSi10Mg alloy processed by selective laser melting, J. Alloys Compd. 798 (2019) 644–655, https://doi.org/10.1016/j.jallcom.2019.05.279.
[31] M. Chen, X. Li, G. Ji, Y. Wu, Z. Chen, W. Baekelant, K. Vanmeensel, H. Wang, J.-P. Kruth, Novel composite powders with uniform TiB2 nano-particle distribution for 3D printing, Appl. Sci. 7 (2017) 250, https://doi.org/10.3390/app7030250.
[32] G.E. Totten, D.S. Mackenzie, Handbook of aluminum, in: Physical Metallurgy and Processes - 1st, vol. 1, Marcel Dekker, New York, 2003, in: https://www.routledge.com/Handbook-of-Aluminum-Vol-1-Physical-Metallurgy-and-Processes/Totten-MacKenzie/p/book/9780824704940.
[33] A. Borbély, I. Groma, Variance method for the evaluation of particle size and dislocation density from x-ray Bragg peaks, Appl. Phys. Lett. 79 (2001) 1772–1774.
[34] J. Suryawanshi, K.G. Prashanth, S. Scudino, J. Eckert, O. Prakash, U. Ramamurty, Simultaneous enhancements of strength and toughness in an Al-12Si alloy synthesized using selective laser melting, Acta Mater. 115 (2016) 285–294, https://doi.org/10.1016/j.actamat.2016.06.009.
[35] J. Wu, X.Q. Wang, W. Wang, M.M. Attallah, M.H. Loretto, Microstructure and strength of selectively laser melted AlSi10Mg, Acta Mater. 117 (2016) 311–320, https://doi.org/10.1016/j.actamat.2016.07.012.
[36] N. Takata, M. Liu, H. Kodaira, A. Suzuki, M. Kobashi, Anomalous strengthening by supersaturated solid solutions of selectively laser melted Al–Si-based alloys, Additive Manufacturing 33 (2020) 101152, https://doi.org/10.1016/j.addma.2020.101152.
[37] A. Hadadzadeh, C. Baxter, B.S. Amirkhiz, M. Mohammadi, Strengthening mechanisms in direct metal laser sintered AlSi10Mg: comparison between virgin and recycled powders, Additive Manufacturing 23 (2018) 108–120, https://doi.org/10.1016/j.addma.2018.07.014.
[38] E.O. Hall, The deformation and ageing of mild steel: III discussion of results, in: Proceedings of the Physical Society. Section B., vol. 64, 1951, pp. 747–753, https://doi.org/10.1088/0370-1301/64/9/303.
[39] K.V. Yang, P. Rometsch, C.H.J. Davies, A. Huang, X. Wu, Effect of heat treatment on the microstructure and anisotropy in mechanical properties of A357 alloy produced by selective laser melting, Mater. Des. 154 (2018) 275–290, https://doi.org/10.1016/j.matdes.2018.05.026.
[40] P. Wang, C. Gammer, F. Brenne, T. Niendorf, J. Eckert, S. Scudino, A heat treatable TiB2/Al-3.5Cu-0.5Mg-1Si composite fabricated by selective laser melting: microstructure, heat treatment and mechanical properties, Compos. B Eng. 147 (2018) 162–168, https://doi.org/10.1016/j.compositesb.2018.04.026.
[41] A. Hadadzadeh, B.S. Amirkhiz, M. Mohammadi, Contribution of Mg2Si precipitates to the strength of direct metal laser sintered AlSi10Mg, Mater. Sci. Eng., A 739 (2019) 295–300, https://doi.org/10.1016/j.msea.2018.10.055.